

# Atom-by-Atom Fabrication of Monolayer Molybdenum Membranes

Xiaoxu Zhao, Jiadong Dan, Jianyi Chen, Zijong Ding, Wu Zhou,\* Kian Ping Loh,\* and Stephen J. Pennycook\*

**Fabrication of materials in the monolayer regime to acquire fascinating physical properties has attracted enormous interest during the past decade, and remarkable success has been achieved for layered materials adopting weak interlayer van der Waals forces. However, the fabrication of monolayer metal membranes possessing strong intralayer bonding remains elusive. Here, suspended monolayer Mo membranes are fabricated from monolayer MoSe<sub>2</sub> films via selective electron beam (e-beam) ionization of Se atoms by scanning transmission electron microscopy (STEM). The nucleation and subsequent growth of the Mo membranes are triggered by the formation and aggregation of Se vacancies as seen by atomic resolution sequential STEM imaging. Various novel structural defects and intriguing self-healing characteristics are unveiled during the growth. In addition, the monolayer Mo membrane is highly robust under the e-beam irradiation. It is likely that other metal membranes can be fabricated in a similar manner, and these pure metal-based 2D materials add to the diversity of 2D materials and introduce profound novel physical properties.**

Atomically thin 2D materials have been one of the most extensively studied materials for the past decade. The weak interlayer van der Waals (vdW) forces relative to the strong in-plane covalent bonding is the hallmark of 2D materials.<sup>[1,2]</sup> 2D monolayer metal membranes represent a new class of 2D materials, for which theory reveals fascinating physical properties. For example, enhanced magnetic moments were predicted in monolayer Hf<sup>[3]</sup> and Fe.<sup>[4]</sup> Monolayer Sn membranes are large-gap quantum spin hall insulators suggested by theory.<sup>[5]</sup> In addition, the physical properties are strongly dependent on the precise atomic structure of the monolayer metal membranes. Theoretical calculations reveal that

monolayer honeycomb gold is semiconducting, whereas monolayer close-packed gold is metallic.<sup>[6]</sup> Yet due to the strong metallic bonding in metals, very few reports have demonstrated the fabrication of monolayer metal membranes, either freestanding or on an appropriate secondary substrate.<sup>[3,4]</sup> The electronic structure of the metal membrane is known to be remarkably impacted by the strong coupling with the substrate. So far, one suspended monolayer metal membrane, that is, Fe, has been fabricated inside graphene nanopores, however, the geometry and properties of the Fe membrane are significantly constrained by the graphene nanopores.<sup>[4]</sup>


Atomically focused e-beams in scanning transmission electron microscopy (STEM) have long been used for materials imaging and elemental analysis.<sup>[7]</sup> Recently, it has been further demonstrated as a powerful

tool to engineer and modify atomic structures of 2D materials with atomic precision.<sup>[8,9]</sup> Patterning 1D atomic chains or nanowires,<sup>[10–16]</sup> triggering phase transformations,<sup>[17,18]</sup> and manipulating atom migrations<sup>[9,19]</sup> in 2D materials have been demonstrated by STEM when appropriate energy is transferred from the e-beam to the sample. However, ionizing one specific element in a binary compound to form a suspended monolayer metal membrane via e-beam irradiation in STEM has rarely been reported.

Here, using atomically focused e-beams in STEM, we have successfully fabricated monolayer Mo membranes by selectively ionizing Se atoms in monolayer MoSe<sub>2</sub>.<sup>[12,26]</sup> The relatively

X. X. Zhao, Dr. J. Y. Chen, Dr. Z. J. Ding, Prof. K. P. Loh  
Department of Chemistry  
National University of Singapore  
3 Science Drive 3, Singapore 117543, Singapore  
E-mail: chmlhkp@nus.edu.sg

X. X. Zhao, J. D. Dan, Prof. S. J. Pennycook  
NUS Graduate School for Integrative Sciences and Engineering  
National University of Singapore  
13 Centre for Life Sciences, #05-01, 28 Medical Drive  
Singapore 117456, Singapore  
E-mail: steve.pennycook@nus.edu.sg

 The ORCID identification number(s) for the author(s) of this article can be found under <https://doi.org/10.1002/adma.201707281>.

J. D. Dan, Prof. S. J. Pennycook  
Department of Materials Science and Engineering  
National University of Singapore  
9 Engineering Drive 1, Singapore 117575, Singapore

Prof. W. Zhou  
School of Physical Sciences and CAS Center for Excellence in Topological Quantum Computation  
University of Chinese Academy of Sciences  
Beijing 100049, China  
E-mail: wuzhou@ucas.ac.cn

DOI: 10.1002/adma.201707281

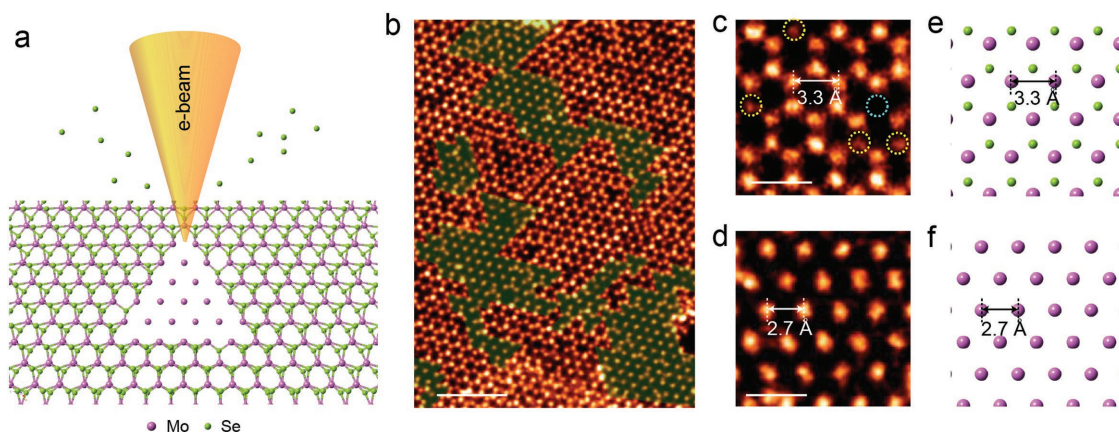


**Figure 1.** e-beam fabrication of monolayer Mo membranes. a) Schematic illustration of the fabrication of a monolayer Mo membrane by selective sputtering of Se atoms from a freestanding monolayer MoSe<sub>2</sub> film. b) STEM-ADF image of as-fabricated Mo membranes embedded in the monolayer MoSe<sub>2</sub> films. Mo membrane regions are highlighted by yellow false color. c,d) STEM-ADF images showing a monolayer MoSe<sub>2</sub> film (c) and monolayer Mo membrane (d). Corresponding in-plane Mo–Mo distances in the monolayer MoSe<sub>2</sub> film (c) and the monolayer Mo membrane (d) are indicated by the white arrows.  $V_{Se}$  and  $V_{Se2}$  are highlighted by the yellow and blue dashed circles, respectively in (c). Atomic models of the monolayer MoSe<sub>2</sub> film (e) and monolayer Mo membrane (f). Scale bars: 2 nm in (b), 0.5 nm in (c, d).

weak Mo–Se bond affords monolayer MoSe<sub>2</sub> as the most appropriate template for growing a Mo membrane compared to MoO<sub>3</sub>, Mo<sub>2</sub>C etc., where the dissociation of Mo–X (X = C, and O) bonds is difficult to be triggered by e-beam irradiation. The size of the as-prepared Mo membranes can reach  $\approx 25$  nm<sup>2</sup>. They retain the close-packed structure of the sandwiched Mo layer in MoSe<sub>2</sub> films, which differs considerably from the body centered cubic (BCC) structure in bulk Mo metal. The as-fabricated Mo membranes are under tensile strain and are further stabilized by the adjacent monolayer MoSe<sub>2</sub> films. The atom-by-atom formation kinetics of Mo membranes is unveiled in real time by sequential STEM imaging. Two precursor states, that is, vacancy complexes and line defects, contribute to the growth of Mo membranes, and both are triggered by the formation and subsequent aggregation of Se vacancies. The as-fabricated Mo membranes are robust under e-beam irradiation and exhibit intriguing self-healing characteristics.

**Figure 1a** schematically illustrates the formation mechanism of monolayer Mo membranes. The selective e-beam ejection of Se atoms is believed to be predominantly triggered by the ionization effect (see Section S1, Supporting Information, for a detailed discussion).<sup>[11,20,21]</sup> The parental monolayer MoSe<sub>2</sub> films were grown by chemical vapor deposition (CVD) under Mo-rich conditions.<sup>[22]</sup> Due to the chalcogen-deficient growth environment, a high density of Se vacancies (Figure S1, Supporting Information) is incorporated in the monolayer film, attributed to the reduced formation energies of Se vacancies.<sup>[20,21,23]</sup> Our experiments indicate that this preexisting high density of Se vacancies is a prerequisite and plays a significant role in the fabrication of monolayer Mo membranes. (See Section S1, Supporting Information, for a detailed discussion.)

A typical STEM-annular dark field (STEM-ADF) image of a monolayer Mo membrane is depicted in Figure 1b, where the Mo membrane regions are highlighted by the yellow false color. The maximum size of the Mo membrane can reach  $\approx 25$  nm<sup>2</sup> (Figure S2, Supporting Information). The parental monolayer MoSe<sub>2</sub> (Figure 1c,e) film reveals a signature

honeycomb structure, with the sandwiched Mo layer taking a close-packed structure.<sup>[22]</sup> Intriguingly, the as-fabricated Mo membrane firmly retains the close-packed structure of the monolayer MoSe<sub>2</sub> film (Figure 1d,f), in contrast to the BCC structure of bulk Mo metal. Density functional calculations show that the most thermodynamically stable lattice constant for the suspended monolayer Mo membrane is  $\approx 2.6$  Å (Figure S3, Supporting Information), which is similar to the experimental value of  $\approx 2.7 \pm 0.05$  Å (for a detailed discussion, see Section S2, Supporting Information). No characteristic carbon or oxygen peaks are found in either monolayer MoSe<sub>2</sub> precursors or monolayer Mo membranes in electron energy loss (EEL) spectra (Figure S4, Supporting Information). In addition, the experimental and theoretical  $d_{Mo-Mo}$  distances in mono- and bilayer AA-stacked Mo<sub>2</sub>C films (Figure S5, Supporting Information) are  $\approx 3.0$  Å,<sup>[24,25]</sup> which are significantly larger than the lattice constant in monolayer Mo membranes. The as-fabricated monolayer Mo membranes are not stable under ambient conditions, as holes have been observed to develop in the membranes after a few hours exposure in air.

White dashed lines in **Figure 2a** highlight the phase boundaries between the monolayer Mo membrane and the parental monolayer MoSe<sub>2</sub> film. The phase boundaries consistently terminate along the Mo-zigzag directions in MoSe<sub>2</sub> or the  $\langle 10\bar{1}0 \rangle$  directions of the Mo membranes regardless of where Mo membranes start to nucleate, thereby the fabrication process is believed to be self-regulating. Mo adatoms (Mo<sub>Mo</sub>) (Figure 2b) and Mo monovacancies ( $V_{Mo}$ ) (Figure 2c) are occasionally found in Mo membranes as corroborated by the intensity line profiles (Figure 2d). They are highly mobile and hop rapidly under the e-beam irradiation. When a  $V_{Mo}$  is produced near a Mo<sub>Mo</sub>, the proximal Mo<sub>Mo</sub> reoccupies the vacancy site rapidly via atomic diffusion (Figure S6, Supporting Information) with energy supplied by the e-beam. The calculated local density of states (LDOS) (Figure S7, Supporting Information) indicates the Mo membrane is metallic, which is consistent with the experimental results that the Mo membrane is highly robust under

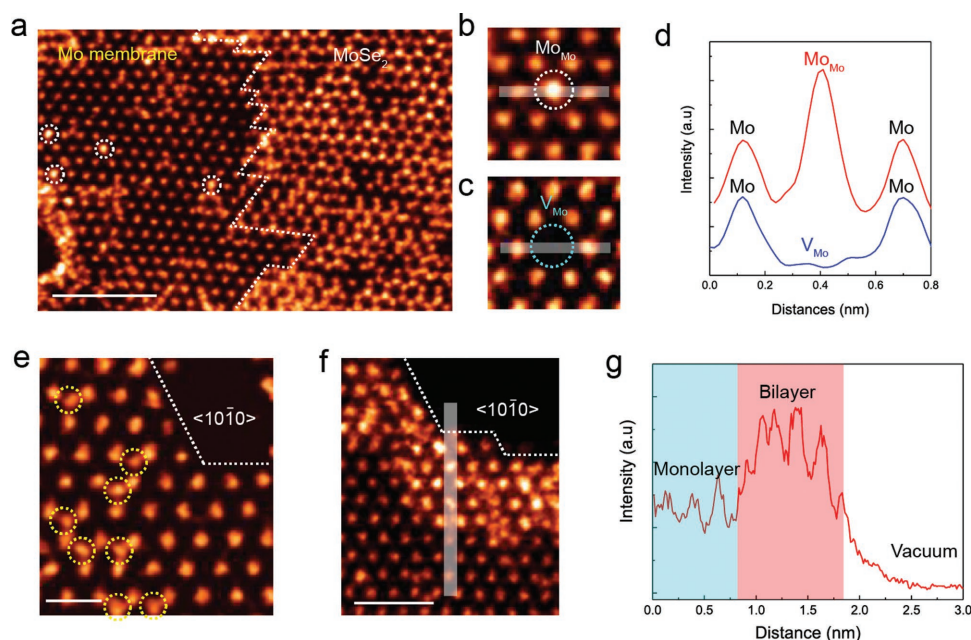


**Figure 2.** Structural properties of the as-fabricated monolayer Mo membrane. a) STEM-ADF image showing phase boundaries (highlighted by the white dashed lines) between the as-fabricated monolayer Mo membrane and parental monolayer MoSe<sub>2</sub> film. b, c) STEM-ADF images of a Mo<sub>Mo</sub> site (b) and a V<sub>Mo</sub> vacancy site in the monolayer Mo membrane (c). d) Intensity line profiles showing the Mo<sub>Mo</sub> (red line) and the V<sub>Mo</sub> (blue line). e) STEM-ADF image depicting exposed atomically sharp edges along the  $\langle 10\bar{1}0 \rangle$  directions as highlighted by the white dashed lines in the monolayer Mo membrane. Remaining Se atoms are highlighted by yellow dashed circles. f) STEM-ADF image of a bilayer Mo membrane, which takes AA stacking registry. g) Intensity line profile revealing the monolayer (cyan) and bilayer (red) regions in (f). Scale bars: 2 nm in (a), 0.5 nm in (e), and 1 nm in (f).

prolonged e-beam irradiations. A detailed discussion is presented below.

The exposed edges of Mo membranes are found exclusively terminating along the  $\langle 10\bar{1}0 \rangle$  directions, whereas the other type of edges, that is,  $\langle 11\bar{2}0 \rangle$  are rarely found, indicating an energetic preference for  $\langle 10\bar{1}0 \rangle$  terminations. Under intense e-beam irradiation, the edge of the monolayer membrane can be folded over to form a bilayer Mo membrane. The resulting initial stacking registry in a bilayer membrane is highly defective (Figure S8a, Supporting Information). However, Mo atoms in the second layer diffuse and self-reconstruct rapidly (Figure S8b, Supporting Information) with energy supplied by the e-beam. Surprisingly, the ultimate stacking registry consistently evolves into a perfect AA stacking as depicted in Figure 2f and Figure S8d (Supporting Information). The image intensity in the AA-stacked region is almost double that of the monolayer region as suggested by the intensity line profiles (Figure 2g).

In transition metal dichalcogenide (TMDC) monolayers, a number of structural defects, for example, atomic defects,<sup>[23]</sup> phase boundaries,<sup>[17]</sup> and mirror twin boundaries,<sup>[26]</sup> have been unveiled in situ during grain inversions or phase transitions. In contrast, various vacancy complexes (highlighted in Figure 3b) agglomerated by a different number of selenium vacancies (marked in Figure 3a) have been observed for the first time during the fabrication of monolayer Mo membranes. Typical examples of selenium vacancy complexes are depicted in Figure 3c–f, including a diselenium vacancy (V<sub>Se2</sub>) (Figure 3c), a vacancy complex of three V<sub>Se2</sub> forming a single Mo dot (V<sub>Se6</sub>) which is the building block for the Mo membranes (Figure 3d), a vacancy complex of six V<sub>Se2</sub> forming a three-atom-size triangular shape Mo membrane

(V<sub>Se12</sub>) (Figure 3e), and a vacancy complex of ten V<sub>Se2</sub> forming a six-atom-size triangular shaped Mo membrane (V<sub>Se20</sub>) (Figure 3f). In parallel, their corresponding atomic models are depicted in the lower panels. All vacancy complexes can be formed by agglomeration of different numbers of V<sub>Se2</sub>, thereby each V<sub>Se2</sub> behaves like a nucleation site, which attracts proximal V<sub>Se2</sub> to segregate and allows Mo membranes to grow larger.

To monitor the actual growth mechanism of Mo membranes in situ, sequential STEM-ADF imaging was employed with each consecutive frame 5 s apart (Movie S1, Supporting Information). Selected snapshots with different irradiation times (0, 5, 10, 25, and 140 s) are depicted in Figure 4a. It is easy to see how the numbers of Se vacancies increase with irradiation time, and simultaneously the lateral size of the Mo membranes is growing. To unveil the growth details at the atomic scale, each V<sub>Se</sub> and V<sub>Se2</sub> sites (Figure 4b) are labeled by yellow and cyan circles, respectively. After 5 s ( $1 \times 10^6 \text{ e}^- \text{ nm}^{-2}$ ) e-beam exposure, one Se atom located at position 4,4 is ionized and correspondingly a V<sub>Se</sub> (highlighted by a solid yellow circle) is created. Intriguingly the Se<sub>2</sub> site at position 4,4 is surrounded by four V<sub>Se</sub> and V<sub>Se2</sub> vacancy sites in total suggesting Se atoms with adjacent Se vacancies are more prone to be ionized.<sup>[27–29]</sup> Upon another 5 s irradiation, one V<sub>Se</sub> site at position 3,5 loses the other Se atom and transforms into a V<sub>Se2</sub> site, representing the evolution from V<sub>Se</sub> to V<sub>Se2</sub>. With a total 25 s exposure time, four additional V<sub>Se</sub> sites (at position 3,4, 4,4, 4,5, and 5,5) lose their remaining Se atoms, and a V<sub>Se12</sub> vacancy complex is formed. In addition, the inverse transformation from V<sub>Se2</sub> to V<sub>Se</sub> (140 s at position 2,5 and 3,5) induced by the migration of a Se vacancy is also captured. After a total 140 s e-beam



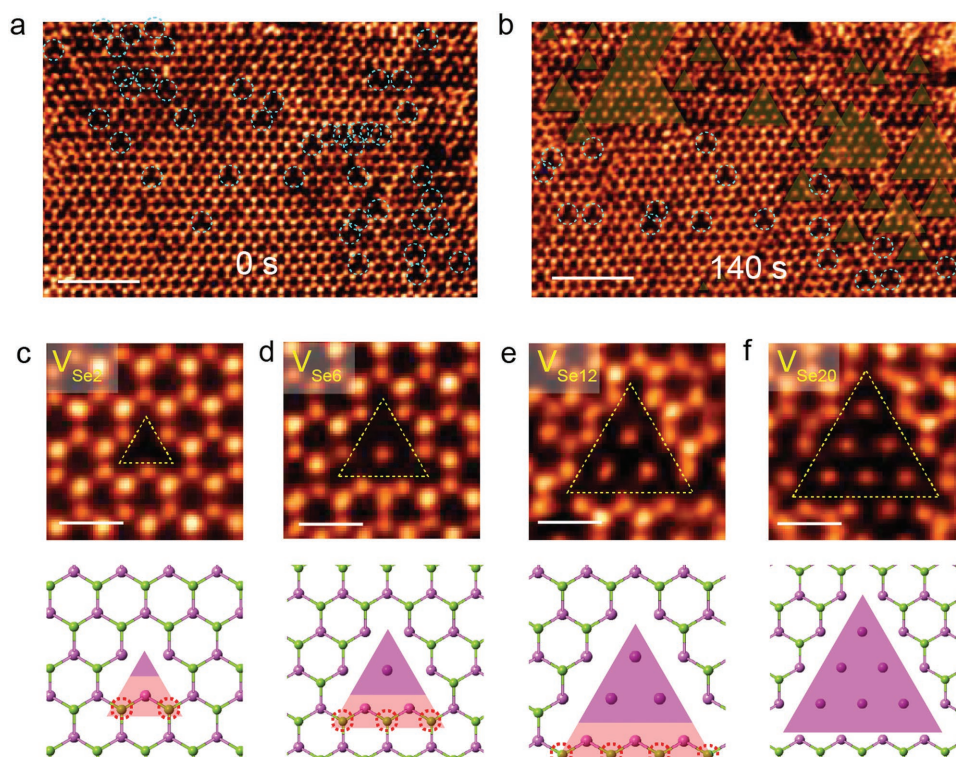


**Figure 3.** Atomic structures of vacancy complexes during the formation of monolayer Mo membranes. a,b) STEM-ADF images of the same region before (a) and after (b) in situ e-beam irradiation for 140 s.  $V_{Se2}$  atomic defects are highlighted by cyan dashed circles in (a), and agglomerated triangular shape  $V_{Se2}$  vacancy complexes are highlighted by blue false color in (b). c–f) STEM-ADF images showing various agglomerated Se vacancy complexes, including: c)  $V_{Se2}$ , d)  $V_{Se6}$ , e)  $V_{Se12}$ , and f)  $V_{Se20}$ , respectively. Corresponding schematic atomic models are depicted in the lower panels. Scale bars: 2 nm in (a, b), 0.5 nm in (c–f).

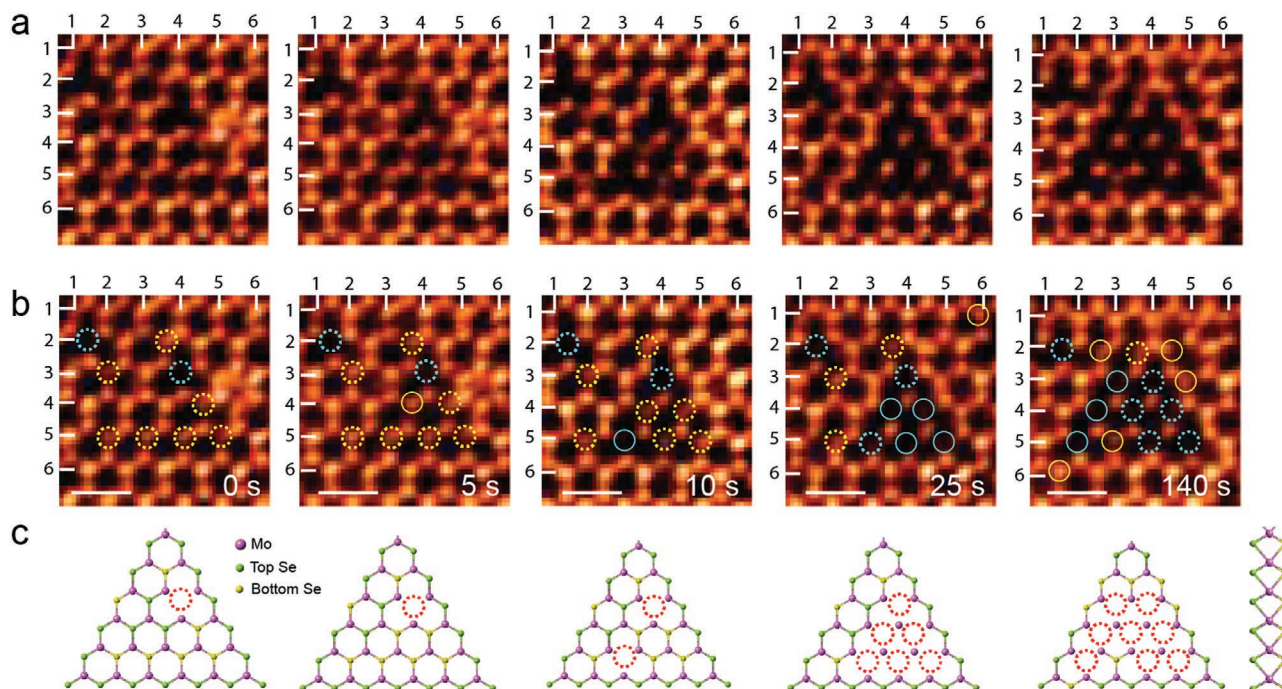


**Figure 4.** In situ sequential STEM-ADF images depicting the step-by-step growth of monolayer Mo membranes via the formation of selenium vacancy complexes. a) Sequential STEM-ADF images of the same region after e-beam irradiation for 0, 5, 10, 25, and 140 s, respectively. b) The same images as (a) where  $V_{Se}$  and  $V_{Se2}$  are highlighted by yellow and blue circles, respectively. The preexisting vacancies are highlighted by dashed circles, whereas the fresh vacancies induced by the e-beam are highlighted by solid circles. c) Corresponding atomic models of (a). Top and bottom layers of Se atoms are shown in green and yellow balls, respectively.  $V_{Se2}$  sites are highlighted by red dashed circles. Scale bars: 0.5 nm.

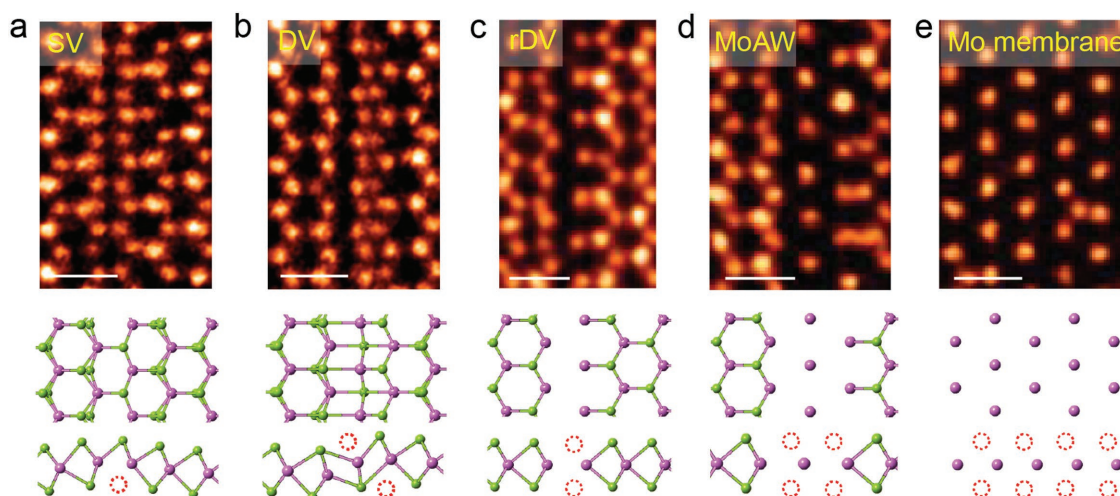


**Figure 5.** Atomic structures of line defects during the formation of monolayer Mo membranes. a–e) STEM-ADF images of: a) SV, b) DV, c) rDV, d) MoAW, and e) Mo membrane, respectively. Corresponding atomic models are depicted in the lower panels. Se line vacancies are highlighted by the red dashed circles. Scale bars: 0.5 nm.

irradiation, an atom-by-atom formation of a six-atom-size triangular shape Mo membrane is monitored in situ (Movie S1, Supporting Information). Hence, we can conclude that the growth of a Mo membrane is triggered by the formation and subsequent migration of Se vacancies. Corresponding atomic models (Figure 4c) at different growth stages are depicted in the lower panels.

Vacancy line defects (Figure 5) are also occasionally involved in the growth of Mo membranes at the early stage, contributing together with vacancy complexes. Single vacancy line defects (SV) and double vacancy line defects (DV) (Figure 5a,b) are well documented in TMDC thin films.<sup>[20,23,26]</sup> Here, we observe reconstructed double vacancy line defects (rDV) (Figure 5c) for the first time, which is formed by integrating two SVs (highlighted in the atomic model) at the same atomic site. In addition, a single Mo atomic wire (MoAW) (Figure 5d) induced by combining two adjacent rDVs is occasionally spotted during the growth. Notably, MoAW is the 1D building block for monolayer Mo membranes when it grows along the  $[11\bar{2}0]$  direction. The actual growth mechanism is predominantly triggered by the formation of vacancy complexes and only occasionally are vacancy line defects involved during the early stage growth (Movie S2, Supporting Information).

During the early stage of growing monolayer Mo membranes, occasionally some Se atoms are ionized together with Mo atoms, leading to the formation of holes (highlighted by white dashed circles in Figure 6a) incorporated inside the semiconducting  $\text{MoSe}_2$  film. Similar ionization effects are commonly observed in various semiconducting TMDC films and have been widely utilized to sculpt novel atomic structures.<sup>[10,11]</sup> Atoms residing at hole regions are prone to be ionized by the e-beam compared to the same atoms located in the interior region;<sup>[11,30,31]</sup> thereby, the holes usually grow larger upon a prolonged e-beam irradiation in semiconducting TMDC films.<sup>[32,33]</sup>

In stark contrast to generating holes in TMDC films,<sup>[32,33]</sup> intriguing self-healing characteristics are observed in these monolayer Mo membranes. After 76 s ( $1.5 \times 10^7 \text{ e}^- \text{ nm}^{-2}$ ) e-beam irradiation, surprisingly the lateral size of the holes (Figure 6b) is remarkably reduced. In parallel, the exposed edges become atomically sharp and exclusively terminate along the  $\langle 10\bar{1}0 \rangle$  directions. The as-fabricated Mo membrane is metallic; thereby, it can rapidly mitigate the ionization damage arising from the inelastic scattering of electrons. In addition, the maximum energy supplied from the e-beam (80 kV) is significantly lower than the knock-on threshold of Mo atoms.<sup>[11]</sup> Hence, prolonged e-beam irradiation only enables excitation of

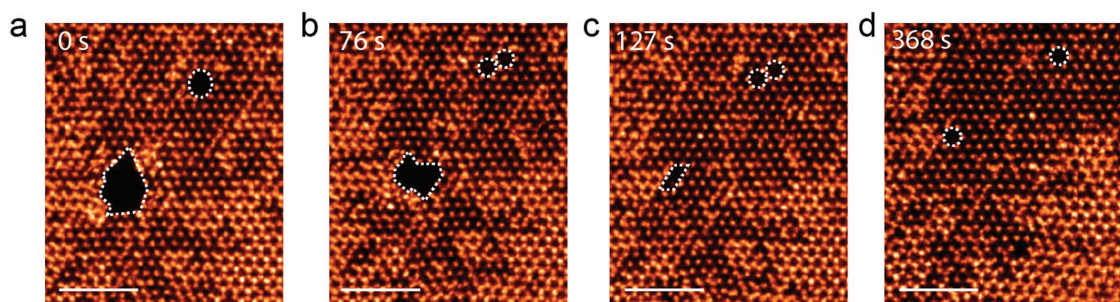


**Figure 6.** Self-healing characteristics of a monolayer Mo membrane. a–d) Sequential STEM-ADF images of the same region after e-beam irradiation for: a) 0, b) 76, c) 127, and d) 368 s, respectively. Holes highlighted by white dashed lines gradually vanish upon prolonged e-beam irradiation. Scale bars: 2 nm.



Mo surface adatoms resulting in redeposition rather than the creation of Mo atomic defects.<sup>[30]</sup>

Upon additional e-beam irradiation ( $127\text{ s}$ ,  $2.5 \times 10^7\text{ e}^- \text{ nm}^{-2}$ ), the surface Mo adatoms are highly mobile and diffuse rapidly over the Mo membrane. They continuously fall into the holes to reduce the total energy of the system. As depicted in Figure 6c, the holes almost fully evolve into single or multiple point defects highlighted by white dashed circles after sufficient energy supply demonstrating self-healing characteristics. The resulting Mo membrane is highly robust under e-beam irradiation as depicted in Figure 6d. After a long time has elapsed ( $368\text{ s}$ ,  $7.4 \times 10^7\text{ e}^- \text{ nm}^{-2}$ ), the as-prepared Mo membranes preserve their structural integrity and no additional defects are created. Instead, atomic defects are seen hopping near the adjacent lattices, validating that the migration of Mo vacancies can be easily triggered by e-beam irradiation.

In conclusion, we have successfully prepared a new atomically thin 2D material, that is, a monolayer Mo membrane, via a top-down method triggered by atomically focused e-beams in STEM. Their formation mechanisms and various novel structural defects are simultaneously captured at the atomic scale. In principle, other types of monolayer metal membranes with fascinating physical properties could be fabricated via a similar approach when appropriate binary compounds and acceleration voltages are chosen. In addition, the as-prepared metal membrane retains the crystal structure of the parent material; thereby, other metal membranes with interesting crystal structures could be delaminated by this e-beam induced top-down method.

## Experimental Section

**MoSe<sub>2</sub> Monolayer Growth:** Monolayer MoSe<sub>2</sub> crystals were grown on a molten soda-lime-silica glass substrate via a CVD method. The detailed methodology can be found in a previous report.<sup>[22]</sup> The selenium powder used for growing Se-deficient MoSe<sub>2</sub> films was 0.6 g, which was almost half of the standard recipe.

**STEM Sample Preparation:** The STEM sample was prepared via the isopropyl alcohol (IPA)-assisted polymer free method.<sup>[34]</sup> Cu quanti-foil transmission electron microscopy (TEM) grids were placed onto the targeted fresh MoSe<sub>2</sub> monolayer films assisted by an optical microscope. A few drops of IPA solvent (99.7%) were carefully dropped to wet the interface between the TEM grid and the MoSe<sub>2</sub> surface. The sample was placed in air for  $\approx 10\text{ min}$  to allow a slow evaporation of the IPA. Subsequently, the sample was placed on a heater at  $100\text{ }^\circ\text{C}$  for  $15\text{ min}$  to ensure all IPA solvent was evaporated, and the TEM grids tightly bonded with the targeted monolayer MoSe<sub>2</sub> films. The MoSe<sub>2</sub> sample together with the TEM grids was immersed in  $1\text{ M}$  KOH solvent for  $6\text{ h}$  to detach it from the soda-lime-silica glass substrate. After etching, TEM grids were rinsed in deionized water ( $5\text{ times} \times 5\text{ min}$ ) and IPA ( $2\text{ times} \times 5\text{ min}$ ), respectively, to remove all KOH residues. Finally, the obtained TEM grids were annealed in an ultrahigh vacuum (UHV) chamber ( $\approx 1 \times 10^{-9}\text{ torr}$ ) at  $180\text{ }^\circ\text{C}$  for  $\approx 12\text{ h}$  to eliminate surface absorbents prior to the STEM characterization.

**STEM Characterization and Image Simulation:** STEM-ADF imaging was carried out on an aberration-corrected JEOL ARM-200F equipped with a cold field emission gun, operating at  $80\text{ kV}$ , and an ASCOR probe corrector. The convergence semiangle of the probe was  $\approx 30\text{ mrad}$ . STEM-ADF images were collected using a half-angle range from  $\approx 85$  to  $280\text{ mrad}$ . A dwell time of  $19\text{ }\mu\text{s pixel}^{-1}$  was set for single-scan imaging, and  $10\text{ }\mu\text{s pixel}^{-1}$  for sequential imaging. Sequential images are aligned by Python scripts to remove the image drift. The imaging dose rate for single-scan imaging is estimated as  $8 \times 10^5\text{ e nm}^{-2}\text{ s}^{-1}$  with a total dose

of  $1.6 \times 10^7\text{ e nm}^{-2}$ , whereas the image dose rate for sequential imaging is estimated as  $2 \times 10^5\text{ e nm}^{-2}\text{ s}^{-1}$  with a total dose of  $4 \times 10^6\text{ e nm}^{-2}$ . Image simulations were done with the QSTEM package assuming an aberration-free probe and  $\approx 1\text{ }\text{\AA}$  source size to give a probe size of  $\approx 1.2\text{ }\text{\AA}$  which provided the best fit to the image.

**DFT Calculations:** Density functional theory (DFT) was employed for first-principles calculations. Projector augmented-wave pseudopotentials<sup>[35]</sup> and the Perdew–Burke–Ernzerhof<sup>[36]</sup> form of the exchange–correlation functional, as implemented in the Vienna ab initio simulation package code<sup>[37]</sup> were used. An energy cutoff of  $280\text{ eV}$  was applied for plane waves and the criterion for total energy convergence was set to  $10^{-4}\text{ eV}$ . All atoms were relaxed during geometry optimization until the magnitude of the forces was less than  $0.04\text{ eV }\text{\AA}^{-1}$ .

## Supporting Information

Supporting Information is available from the Wiley Online Library or from the author.

## Acknowledgements

X.Z. and J.D. contributed equally to this work. K.P.L. thanks MOE Tier 2 grant “Porous, Conjugated Molecular Framework for Energy Storage” (MOE2016-T2-1-003) and also funding by SinBeRISE CREATE, National Research Foundation, Prime Minister’s Office. W.Z. acknowledges support from the CAS Pioneer Hundred Talents Program and the Natural Science Foundation of China (51622211). S.J.P. is grateful to the National University of Singapore for funding.

## Conflict of Interest

The authors declare no conflict of interest.

## Keywords

2D materials, in situ phase transformation, monolayer metal membrane, structural defects

Received: December 13, 2017

Revised: March 6, 2018

Published online: April 30, 2018

- [1] M. Chhowalla, H. S. Shin, G. Eda, L.-J. Li, K. P. Loh, H. Zhang, *Nat. Chem.* **2013**, *5*, 263.
- [2] K. S. Novoselov, A. K. Geim, S. V. Morozov, D. Jiang, Y. Zhang, S. V. Dubonos, I. V. Grigorieva, A. A. Firsov, *Science* **2004**, *306*, 666.
- [3] L. Li, Y. Wang, S. Xie, X. Bin Li, Y. Q. Wang, R. Wu, H. Sun, S. Zhang, H. J. Gao, *Nano Lett.* **2013**, *13*, 4671.
- [4] J. Zhao, Q. Deng, A. Bachmatiuk, G. Sandeep, A. Popov, J. Eckert, M. H. Rummeli, *Science* **2014**, *343*, 1228.
- [5] Y. Xu, B. Yan, H. J. Zhang, J. Wang, G. Xu, P. Tang, W. Duan, S. C. Zhang, *Phys. Rev. Lett.* **2013**, *111*, 136804.
- [6] N. Liu, S. Jin, L. Guo, G. Wang, H. Shao, L. Chen, X. Chen, *Phys. Rev. B* **2017**, *95*, 155311.
- [7] O. L. Krivanek, M. F. Chisholm, V. Nicolosi, T. J. Pennycook, G. J. Corbin, N. Dellby, M. F. Murfitt, C. S. Own, Z. S. Szilagyi, M. P. Oxley, S. T. Pantelides, S. J. Pennycook, *Nature* **2010**, *464*, 571.
- [8] X. Zhao, J. Kotakoski, J. C. Meyer, E. Sutter, P. Sutter, A. V. Krashenninnikov, U. Kaiser, W. Zhou, *MRS Bull.* **2017**, *42*, 667.

- [9] O. Dyck, S. Kim, S. V. Kalinin, S. Jesse, *Appl. Phys. Lett.* **2017**, *111*, 4998599.
- [10] J. Lin, Y. Zhang, W. Zhou, S. T. Pantelides, *ACS Nano* **2016**, *10*, 2782.
- [11] J. Lin, O. Cretu, W. Zhou, K. Suenaga, D. Prasai, K. I. Bolotin, N. T. Cuong, M. Otani, S. Okada, A. R. Lupini, J. C. Idrobo, D. Caudel, A. Burger, N. J. Ghimire, J. Yan, D. G. Mandrus, S. J. Pennycook, S. T. Pantelides, *Nat. Nanotechnol.* **2014**, *9*, 436.
- [12] O. Cretu, H. P. Komsa, O. Lehtinen, G. Algara-Siller, U. Kaiser, K. Suenaga, A. V. Krasheninnikov, *ACS Nano* **2014**, *8*, 11950.
- [13] X. Liu, T. Xu, X. Wu, Z. Zhang, J. Yu, H. Qiu, J. H. Hong, C. H. Jin, J. X. Li, X. R. Wang, L. T. Sun, W. Guo, *Nat. Commun.* **2013**, *4*, 2803.
- [14] Z. Xiao, J. Qiao, W. Lu, G. Ye, X. Chen, Z. Zhang, W. Ji, J. Li, C. Jin, *Nano Res.* **2017**, *10*, 2519.
- [15] V. Vierimaa, A. V. Krasheninnikov, H.-P. Komsa, *Nanoscale* **2016**, *8*, 7949.
- [16] C. Jin, F. Lin, K. Suenaga, S. Iijima, *Phys. Rev. Lett.* **2009**, *102*, 195505.
- [17] Y. C. Lin, D. O. Dumcenco, Y. S. Huang, K. Suenaga, *Nat. Nanotechnol.* **2014**, *9*, 391.
- [18] E. Sutter, Y. Huang, H. P. Komsa, M. Ghorbani-Asl, A. V. Krasheninnikov, P. Sutter, *Nano Lett.* **2016**, *16*, 4410.
- [19] T. Susi, J. C. Meyer, J. Kotakoski, *Ultramicroscopy* **2017**, *180*, 163.
- [20] H. P. Komsa, A. V. Krasheninnikov, *Phys. Rev. B* **2015**, *91*, 125304.
- [21] O. Lehtinen, H. P. Komsa, A. Pulkkin, M. B. Whitwick, M. W. Chen, T. Lehnert, M. J. Mohn, O. V. Yazyev, A. Kis, U. Kaiser, A. V. Krasheninnikov, *ACS Nano* **2015**, *9*, 3274.
- [22] J. Chen, X. Zhao, S. J. R. Tan, H. Xu, B. Wu, B. Liu, D. Fu, W. Fu, D. Geng, Y. Liu, W. Liu, W. Tang, L. Li, W. Zhou, T. C. Sum, K. P. Loh, *J. Am. Chem. Soc.* **2017**, *139*, 1073.
- [23] W. Zhou, X. Zou, S. Najmaei, Z. Liu, Y. Shi, J. Kong, J. Lou, P. M. Ajayan, B. I. Yakobson, J. C. Idrobo, *Nano Lett.* **2013**, *13*, 2615.
- [24] D. Geng, X. Zhao, L. Li, P. Song, B. Tian, W. Liu, J. Chen, D. Shi, M. Lin, W. Zhou, K. P. Loh, *2D Mater.* **2017**, *4*, 011012.
- [25] D. Geng, X. Zhao, Z. Chen, W. Sun, W. Fu, J. Chen, W. Liu, W. Zhou, K. P. Loh, *Adv. Mater.* **2017**, *10*, 1700072.
- [26] J. Lin, S. T. Pantelides, W. Zhou, *ACS Nano* **2015**, *9*, 5189.
- [27] H. P. Komsa, J. Kotakoski, S. Kurasch, O. Lehtinen, U. Kaiser, A. V. Krasheninnikov, *Phys. Rev. Lett.* **2012**, *109*, 035503.
- [28] J. Kotakoski, C. H. Jin, O. Lehtinen, K. Suenaga, A. V. Krasheninnikov, *Phys. Rev. B* **2010**, *82*, 113404.
- [29] A. V. Krasheninnikov, F. Banhart, J. X. Li, A. S. Foster, R. M. Nieminen, *Phys. Rev. B* **2005**, *72*, 125428.
- [30] R. F. Egerton, *Ultramicroscopy* **2013**, *127*, 100.
- [31] R. F. Egerton, P. Li, M. Malac, *Micron* **2004**, *35*, 399.
- [32] R. Zan, Q. M. Ramasse, R. Jalil, T. Georgiou, U. Bangert, K. S. Novoselov, *ACS Nano* **2013**, *7*, 10167.
- [33] G. Algara-Siller, S. Kurasch, M. Sedighi, O. Lehtinen, U. Kaiser, *Appl. Phys. Lett.* **2013**, *103*, 4830036.
- [34] W. Regan, N. Alem, B. Alemán, B. Geng, Ç. Girit, L. Maserati, F. Wang, M. Crommie, A. Zettl, *Appl. Phys. Lett.* **2010**, *96*, 3337091.
- [35] P. E. Blöchl, *Phys. Rev. B* **1994**, *50*, 17953.
- [36] J. Perdew, K. Burke, M. Ernzerhof, *Phys. Rev. Lett.* **1996**, *77*, 3865.
- [37] G. Kresse, J. Hafner, *Phys. Rev. B* **1993**, *47*, 558.